

## Journal Pre-proof

Towards Reduced Order Models via Robust Proper Orthogonal Decomposition to capture personalised aortic haemodynamics

Chotirawee Chatpattanasiri, Gaia Franzetti, Mirko Bonfanti,  
Vanessa Diaz-Zuccarini, [Stavroula Balabani](#)



PII: S0021-9290(23)00329-9  
DOI: <https://doi.org/10.1016/j.jbiomech.2023.111759>  
Reference: BM 111759

To appear in: *Journal of Biomechanics*

Accepted date : 7 August 2023

Please cite this article as: C. Chatpattanasiri, G. Franzetti, M. Bonfanti et al., Towards Reduced Order Models via Robust Proper Orthogonal Decomposition to capture personalised aortic haemodynamics. *Journal of Biomechanics* (2023), doi: <https://doi.org/10.1016/j.jbiomech.2023.111759>.

This is a PDF file of an article that has undergone enhancements after acceptance, such as the addition of a cover page and metadata, and formatting for readability, but it is not yet the definitive version of record. This version will undergo additional copyediting, typesetting and review before it is published in its final form, but we are providing this version to give early visibility of the article. Please note that, during the production process, errors may be discovered which could affect the content, and all legal disclaimers that apply to the journal pertain.

© 2023 Published by Elsevier Ltd.

# Towards Reduced Order Models via Robust Proper Orthogonal Decomposition to Capture Personalised Aortic Haemodynamics

Chotirawee Chatpattanasiri<sup>a</sup>, Gaia Franzetti<sup>a</sup>, Mirko Bonfanti<sup>a</sup>, Vanessa Diaz-Zuccarini<sup>a,b</sup>, Stavroula Balabani<sup>a,\*</sup>

<sup>a</sup>Department of Mechanical Engineering, University College London, London, UK

<sup>b</sup>Wellcome/EPSCRC Centre for Interventional and Surgical Sciences (WEISS), Department of Medical Physics and Biomedical Engineering, University College London, London, UK

## Abstract

Data driven, reduced order modelling has shown promise in tackling the challenges associated with computational and experimental hemodynamic models. In this work, we focus on the use of Reduced Order Models (ROMs) to reconstruct velocity fields in a patient-specific dissected aorta, with the objective being to compare the ROMs obtained from Robust Proper Orthogonal Decomposition (RPOD) to those obtained from the traditional Proper Orthogonal Decomposition (POD). POD and RPOD are applied to in vitro, hemodynamic data acquired by Particle Image Velocimetry and compare the decomposed flows to those derived from Computational Fluid Dynamics (CFD) data for the same geometry and flow conditions. In this work, PIV and CFD results act as surrogates for clinical haemodynamic data eg. MR, helping to demonstrate the potential use of ROMs in real clinical scenarios. The flow is reconstructed using different numbers of POD modes and the flow features obtained throughout the cardiac cycle are compared to the original Full Order Models (FOMs).

Robust Principal Component Analysis (RPCA), the first step of RPOD, has been found to enhance the quality of PIV data, allowing POD to capture most of the kinetic energy of the flow in just two modes similar to the numerical data that are free from measurement noise. The reconstruction errors differ along the cardiac cycle with diastolic flows requiring more modes for accurate reconstruction. In general, modes 1-10 are found sufficient to represent the flow field. The results demonstrate that the coherent structures that characterise this aortic dissection flow are described by the first few POD modes suggesting that it is possible to represent the macroscale behaviour of aortic flow in a low-dimensional space; thus significantly simplifying the problem, and allowing for more computationally efficient flow simulations or machine learning based flow predictions that can pave the way for translation of such models to the clinic.

**Keywords:** Aortic Haemodynamics, Particle Image Velocimetry, Computational Fluid Dynamics, Reduced Order Model, Proper Orthogonal Decomposition, Robust Principle Component Analysis, Patient-specific modelling

## Corresponding author detail

### Stavroula Balabani

Stavroula obtained a Diploma in Chemical Engineering from the National Technical University of Athens in 1989. After a brief career in industry, she joined King's College London in 1993 as a Research Assistant to work on an EU funded project investigating the effects of fouling on heat exchangers in lignite utility boilers. She was awarded the PhD in 1996 and was appointed as a Lecturer in the Department of Mechanical Engineering at King's College London in the same year. During her PhD studies she applied optical diagnostic techniques such as LDA and liquid crystal thermography to resolve the flow and heat transfer characteristics of model tube bundle heat exchangers. She also worked closely with CFD modellers and the power generation industry in order to understand and predict ash fouling. Stavroula was promoted to Senior Lecturer and

Reader in 2005 and 2009 respectively. She also led the fluids group (ECLAT) from October 2009 until her departure from King's in March 2011 to join UCL as a Reader in Thermofluids.

\*Corresponding author

## 1 Introduction

Restoring flow and functionality is the main objective of clinicians when performing vascular interventions. The ability to visualize biomechanical flows, either by *in vitro* experiments or Computational Fluid Dynamics (CFD), can provide invaluable information for clinical support, disease progression predictions and surgical treatment planning (Bonfanti et al., 2020) by helping design tailored interventions, personalise devices or explore clinical scenarios for future treatment, for example. Application of such tools has been successfully demonstrated in several pathologies, such as aortic dissection (Bonfanti et al., 2020; Franzetti et al., 2022; Stokes et al., 2021, 2023), coronary artery disease (Javadzadegan et al., 2018), valve prosthesis (Hellmeier et al., 2018), aortic aneurysm (Febina et al., 2018) and congenital heart disease (Rigatelli et al., 2021). Both *in vitro* and *in silico* hemodynamic approaches are subject to certain limitations. In CFD for example, a compromise between model accuracy and complexity has often need to be made (Bonfanti et al., 2018). Over-simplifications of the geometrical domain and boundary conditions can lead to non-realistic results. However, increasing the model complexity further complicates the solution, increasing the computational time and often introducing or increasing uncertainty. High computational cost represents a problem for the clinical translation of these numerical models, especially when considering the time-scales of *acute* pathological stages (i.e. days rather than weeks or months) and the limited time available in clinics to make full use of CFD as realistic tool for pre-interventional planning.

To address this problem, Reduced Order Models (ROMs) have been extensively studied to accelerate calculations of fluid dynamic problems (Quarteroni and Rozza, 2007). ROMs replace large-scale problems with less complex ones that can be solved with significantly less time and resources, while maintaining acceptable accuracy. [If we were able to extract ROMs from clinical measurement modalities \(e.g MR\) with a view to use them as input to train fast hemodynamic tools this would address the limitations of traditional CFD and completely transform the use of simulation tools for haemodynamic computations in the clinic.](#) Many methods have been developed to extract ROMs from high-fidelity data, such as Proper Orthogonal Decomposition (POD) (Liang et al., 2002; Brunton and Kutz, 2019; Arzani and Dawson, 2021), Proper Generalized Decomposition (PGD) (Chinesta et al., 2011), Dynamic Mode Decomposition (Arzani and Dawson, 2021; Schmid, 2021), Krylov subspace (Farahbakhsh, 2020), and the recently developed neural network based method, Autoencoder (Wang et al., 2016; Murata et al., 2020; Eivazi et al., 2022; Liang et al., 2020).

Among these methods, POD is arguably the most popular <sup>1</sup>. POD reduces the dimensionality of a system by projecting it onto a set of orthogonal Reduced Basis (POD modes). It identifies the dominant modes in a flow, breaking it down into large and small-scale structures. With the goal of quantifying different flow regimes and developing computationally-efficient ROMs, POD has been applied to several vascular flow studies, either using numerical CFD data or experimentally-derived velocity fields acquired via Particle Image Velocimetry (PIV). For instance, Kefayati and Poepping (2013) used a combination of PIV and POD to study transitional flows in stenosed silicon models; Byrne et al. (2014) introduced entropy to quantify the flow instability of intracranial aneurysm using POD; Ballarin et al. (2016) developed a framework for the study of haemodynamics in three-dimensional patient-specific configurations of coronary artery bypass grafts. More recently, Di Labbio and Kadem (2019) compared POD and DMD reconstructions of *in vitro* ventricular flow in a healthy left ventricle and multiple severities of aortic regurgitation, and Han et al. (2020) applied POD to estimate the flow-induced WSS in computational models of abdominal aortic aneurysm.

<sup>1</sup>POD is mathematically equivalent to Principal Component Analysis (PCA) (Liang et al., 2002).

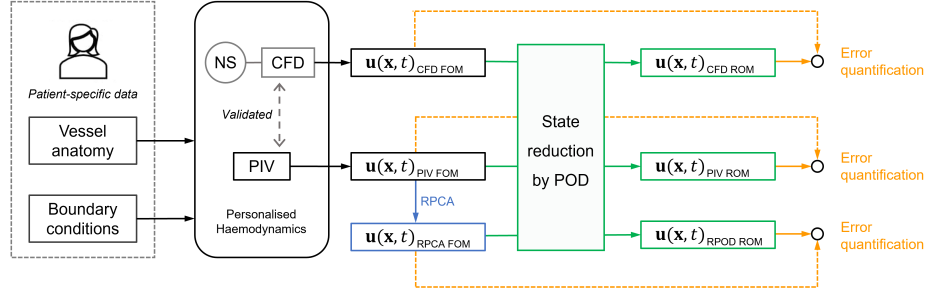


Figure 1: Schematic of the approach followed in this work, comprising four phases. First, the development of Full order models (FOMs), was described in previous works by the authors (Bonfanti et al., 2020; Franzetti et al., 2022) and led to the experimental PIV model and a computational CFD one (black part of the figure.) In the second phase, RPCA is applied to the PIV velocity field to create a de-noised RPCA velocity field (blue part of the figure.) The third phase involves the creation of ROMs based on the original velocity fields through POD (green part of the figure.) In the last phase, the reconstructed velocity fields were compared to their respective original FOMs, the errors involved were assessed (yellow part of the figure.)

Robust Proper Orthogonal Decomposition (RPOD) or Robust Principal Component Analysis (RPCA) is an extension of the Proper Orthogonal Decomposition (POD) method, designed to handle noisy or corrupted data commonly found in clinical and experimental datasets (Arzani and Dawson, 2021; Scherl et al., 2020). However, its application in fluid flows, especially in the field of physiological flows, is limited. Previous studies include Scherl et al. (2020), who implemented RPOD filtering in a turbulent channel flow simulation to extract coherent flow structures from the de-noised low-rank matrix, and Baghaie (2019), who applied RPOD to filter out background motion from raw PIV sequences.

In this work, and in the context of using ROMs for clinical application, we will use PIV and CFD results as surrogates for clinical haemodynamic data to demonstrate the potential of the RPOD algorithm when compared to traditional POD for decomposing aortic flow data and constructing ROMs. The RPOD method was applied to the patient-specific aortic, PIV-derived, flow field described in our previous work (Bonfanti et al., 2020; Franzetti et al., 2022). The eigenflows generated are compared to those derived by POD applied to the same data set as well as CFD-derived flow fields for the same geometry. ROMs are then successfully used to reconstruct the original flow fields and their potential for personalised hemodynamic modelling is discussed.

## 2 Materials and Methods

A schematic of the approach followed in this work is shown in Figure 1. We have previously characterised and fully validated the flow in a patient-specific dissected aorta both experimentally (using PIV) and numerically (using CFD) (Franzetti et al., 2022; Bonfanti et al., 2020) (black part of the



figure). These datasets comprise the Full Order Models. The RPCA algorithm was applied to the PIV velocity field to create a de-noised dataset, which we call RPCA velocity field (blue part of the figure.)

The state reduction of the problem was then achieved by projecting the CFD, PIV, and RPCA velocity fields onto their POD bases to reduce the dimensionality of the problem (Galerkin projection.) ROMs were identified, ROM-derived flow fields were reconstructed (green part of the figure) and compared to the FOMs. The errors introduced when considering a lower dimensional model were assessed (Yellow part of the figure.)

## 2.1 Patient-specific model

The study is based on clinical data acquired from an adult male with a Type B aortic dissection, a pathology that occurs when a tear in the vessel wall allows blood to flow within the layers of the aorta, leading to the formation of two separate flow-channels, the true and the false lumen. The aortic model was created from the patient CT scans using a semi-automated segmentation tool based on thresholding operations, implemented in ScanIP (Synopsys, Mountain View, CA, USA). It includes one inlet and four outlets: the brachiocephalic trunk (BT), left common carotid (LCC), left subclavian artery (LSA), and descending aorta (DA). A rigid, transparent phantom was manufactured by 3D printing technology (Materialise, Belgium) to enable the flow field measurements described below.

## 2.2 Experimental setup and PIV measurements

The phantom was connected to a custom-made pulsatile flow circuit which comprised a computer controlled pulsatile pump and left ventricle simulator, tunable 3-element Windkessel (3WKs) model at each aortic outlet (Figure 2) and an atrial reservoir (Franzetti et al., 2019). The mock loop components were informed by clinical data to reproduce personalised, accurate haemodynamics (Franzetti et al., 2022). A blood mimicking fluid comprising a potassium thiocyanate (KSCN) water solution (63% by weight) was used, matching the refractive index of the phantom. Patient-specific flow and pressure waveforms were introduced at the inlets and outlets of the aortic model as illustrated in (Bonfanti et al., 2020; Franzetti et al., 2022). To perform the PIV measurements, the flow was seeded with fluorescent microparticles with a mean diameter of  $10\ \mu\text{m}$ , injected into the flow upstream of the phantom and allowed to disperse uniformly within the aortic model. The flow was illuminated by a pulsed Nd:YAG laser (Litron Lasers, Bernoulli, UK) emitting 532 nm wavelength light. Particle image pairs were acquired with a CCD camera (Imperx, USA) at a sampling rate of 22 Hz (the pulsatile flow has a frequency of 1.2 Hz) with a resolution of  $4000 \times 3000$  pixels with a time interval of 1ms. 10 cardiac cycles<sup>2</sup>. Velocity fields were generated using the Fast Fourier transform based cross-correlation algorithm, implemented with a three-pass technique starting with an interrogation area of  $64 \times 64$  pixels and ending with an area of  $32 \times 32$  pixels, overlapping by 50%. Lastly, post-processing was performed using custom developed MATLAB (MathWorks Inc., USA) functions. The measurement error, estimated from mass conservation, is 5.32% (Franzetti et al., 2022).

Details about the components of the mock circulatory loop and the experimental procedures can be found in our previous work (Franzetti et al., 2019, 2022). Here, the PIV-derived velocities obtained on a cross-sectional plane of the aortic arch (shown in Figure 2), consisting of 10 cardiac cycles with 18 snapshots per cycle, i.e. 180 snapshots in total, were used. This minimises the risk of bias introduced by using a single cycle, and better represents flow behaviour.

<sup>2</sup>were recorded and the flow converged with less than 1.6% cycle-to-cycle variation (Bonfanti et al., 2020; Franzetti et al., 2022).

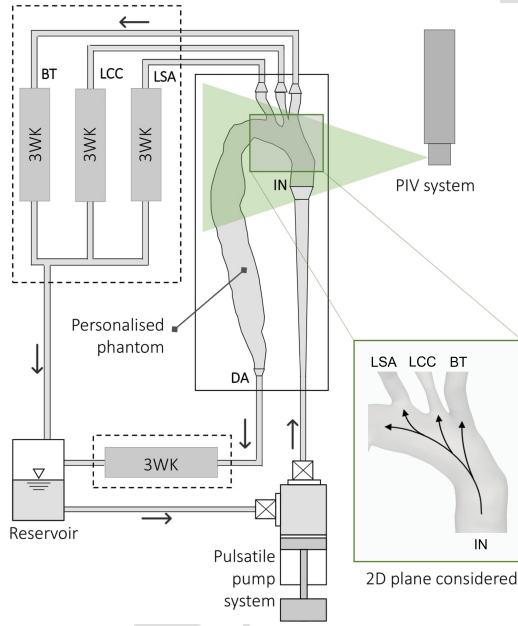


Figure 2: Schematic of the experimental setup. The rig comprises a pulsatile pump system to provide the patient-specific inlet flow rate into the aortic phantom; four 3-elements Windkessel models (3WKs) – one for each of the outlets: brachiocephalic trunk (BT), left common carotid (LCC), left subclavian artery (LSA), and descending aorta (DA) – and an aortic reservoir. The 2D plane where the PIV acquisitions considered in this work were performed is also represented. Superimposed arrows qualitatively indicate the direction of the flow during systole.

### 104 2.3 PIV data enhancement by RPCA

105 Robust Principal Component Analysis (RPCA) or Robust Proper Orthogonal Decomposition (RPOD)  
 106 is an extension of PCA or POD that separate an original data matrix ( $\mathbf{U}$ ) into a sparse noise matrix  
 107 ( $\mathbf{S}$ ) and a low-rank matrix containing coherent information ( $\mathbf{L}$ ) using the following equation:

$$\mathbf{U} = \mathbf{L} + \mathbf{S}. \quad (1)$$

108 RPCA is known for its ability to handle noisy data (Scherl et al., 2020; Arzani and Dawson, 2021;  
 109 Candès et al., 2011; Brunton and Kutz, 2019) and is a good candidate to enhance the PIV data prior to  
 110 further analysis. The implementation of RPCA involves solving a constrained minimization equation:

$$\min_{\mathbf{L}, \mathbf{S}} ( \text{rank}(\mathbf{L}) + \|\mathbf{S}\|_0 ) \text{ subject to } \mathbf{U} = \mathbf{L} + \mathbf{S} \quad (2)$$

111 where  $\|\mathbf{S}\|_0$  represents the zero norm of  $\mathbf{S}$ , which is the summation of non-zero elements in  $\mathbf{S}$ . A convex  
 112 relaxation 2 form of the problem is used:

$$\min_{\mathbf{L}, \mathbf{S}} ( \|\mathbf{L}\|_* + \lambda_0 \|\mathbf{S}\|_1 ) \text{ subject to } \mathbf{U} = \mathbf{L} + \mathbf{S} \quad (3)$$

113 where  $\|\mathbf{L}\|_*$  represents the nuclear norm of  $\mathbf{L}$ , which is the summation of all the singular values of  $\mathbf{L}$ ,  
 114 and  $\|\mathbf{S}\|_1$  denotes the first norm of  $\mathbf{S}$ .  $\lambda_0$  is a hyperparameter introduced as part of the relaxation  
 115 given by  $\lambda_0 = \lambda_1 / \sqrt{\max(m, n)}$  where  $m \times n$  is the dimension of  $\mathbf{U}$  and  $\lambda_1 = 1$  in the original paper  
 116 (Candès et al., 2011). Scherl et al. (2020) suggested that  $\lambda_1$  can also be used as a tuning parameter:  
 117 high  $\lambda_1$  yields high sparsity of  $\mathbf{S}$ , and low  $\lambda_1$  gives low rank of  $\mathbf{L}$ . For simplicity,  $\lambda_1$  is kept at 1 in this  
 118 study. Equation 3 can be solved using the Augmented Lagrange Multiplier (ALM) algorithm together  
 119 with the Alternating Direction Method (ADM) Brunton and Kutz (2019).

120 RPCA is used here as a de-noising tool to improve the PIV velocity field and thus is not applied to  
 121 the CFD data. It is important to note that, because RPCA distinguishes outliers from coherent data,  
 122 it may struggle when data points are scarce, blurring the difference between outliers and coherent  
 123 information. Therefore, all acquired PIV snapshots (180) were used.

124 The term ‘RPCA velocity field’ is used to denote the PIV velocity field that has been de-noised by  
 125 the RPCA process, whereas the term ‘RPOD’ refers to the implementation of POD after RPCA.

### 126 2.4 Numerical simulation

127 The CFD data is taken from a previous study by our group (Bonfanti et al., 2020). A Reynolds-averaged  
 128 Navier–Stokes (RANS) model was employed in this study to match the experimental inlet conditions  
 129 since it is very difficult to achieve truly laminar flow in experiments. While RANS models are known  
 130 to present certain limitations, such as not capturing unsteady turbulence fluctuations and assuming  
 131 fully turbulent flow, they offer a good compromise between accuracy and computational efficiency in  
 132 comparison to more resource-intensive methods like Large Eddy Simulation (LES) and Direct Numer-  
 133 ical Simulation (DNS); they were hence selected for this study and showed good agreement with the  
 134 experimental data (Bonfanti et al., 2020). ANSYS-CFX 19.0 (ANSYS, USA) was used to solve the  
 135 3D incompressible Navier–Stokes and continuity equations, simulating the flow conditions of the PIV  
 136 experiment. The vessel geometry is the same as the one used to make the phantom, with the walls  
 137 assumed rigid. All boundary conditions are set to match those from the experiments. The experi-  
 138 mental inlet flow rate waveform is imposed with a flat velocity profile. 3WKs model is coupled at the

outlets. The fluid is assumed to be Newtonian, with the properties of the KSCN solution. The shear stress transport (SST) turbulence model is chosen with the turbulence intensity of 1% prescribed at the inlet.

The simulations run for 3 cardiac cycles and the first two cycles were excluded from the analysis as they contain transient behaviour influenced by the initial conditions and numerical setup. Unlike in the flow field obtained from PIV experiments, in the case of CFD, once the simulations have converged to the periodic steady state, every cycle is identical. Therefore, a single cycle is used in our study as is commonly done in most patient specific simulations (Bonfanti et al., 2020; Stokes et al., 2023). The flow field on the 2D aortic arch plane corresponding to the experimental one used here was exported to MATLAB via CFD-Post (ANSYS).

## 2.5 Proper Orthogonal Decomposition

The POD method decomposes the flow into a set of *modes* arranged depending on their energy content. The higher energy modes represent the coherent structures in the flow; as a result POD has been applied widely to turbulent flows to extract dominant structures. A detailed description of POD can be found in Berkooz et al. (1993) and in the textbook by Brunton and Kutz (2019). Only a brief overview is provided here.

POD is implemented using the method of *snapshots*. Consider a 2D velocity field of  $n = N_x \times N_y$  spatial velocity vectors  $(u, v)$  on a Cartesian grid  $x, y$  and a total number of  $m$  instantaneous velocity fields or *snapshots*. POD decomposes the fluctuating part of the velocity field  $\mathbf{u}'(x, y, t)$  into a set of spatial functions  $\Phi_i(x, y)$ , called the *POD modes*, weighted by time-dependent coefficients  $a_i(t)$  so that:

$$\mathbf{u}'(x, y, t) = \sum_{i=1}^N a_i(t) \Phi_i(x, y) \quad (4)$$

where  $i$  denotes the mode number, and  $N$  denotes the total number of modes.<sup>3</sup>

To perform the decomposition (Equation 4), the time-averaged velocity  $\mathbf{u}(x, y)$  is first subtracted from each instantaneous velocity field, obtaining a set of  $m$  fluctuating velocity fields  $\mathbf{u}'(x, y, t)$ . The dataset is then rearranged in a  $2n \times m$  *snapshot matrix*  $\mathbf{U}$ :

$$\mathbf{U} = \begin{pmatrix} u'_{1,1} & u'_{1,2} & \cdots & u'_{1,m} \\ \vdots & \vdots & \ddots & \vdots \\ u'_{n,1} & u'_{n,2} & \cdots & u'_{n,m} \\ v'_{1,1} & v'_{1,2} & \cdots & v'_{1,m} \\ \vdots & \vdots & \ddots & \vdots \\ v'_{n,1} & v'_{n,2} & \cdots & v'_{n,m} \end{pmatrix} \quad (5)$$

and Singular Value Decomposition (SVD) is applied:

$$\mathbf{U} = \Phi \Sigma \Psi^* \quad (6)$$

where  $\Phi$  and  $\Psi$  are the left and right singular vectors of  $\mathbf{U}$ , respectively and the singular matrix ( $\Sigma$ ) contains the singular values ( $\sigma_i$ ) of  $\mathbf{U}$ . The latter rank in descending order, and are directly linked to

<sup>3</sup>Note that  $\mathbf{u}'$  in Equation 4 includes both the periodic variation around the mean and the turbulence fluctuation.

the portion of kinetic energy ( $\lambda_i$ ) contained in the POD modes ( $\Phi_i$ ), i.e.  $\lambda_i = \sigma_i^2$ . Therefore, POD modes are ranked according to their energy content, with the first mode having the highest energy, and the last the lowest. The energy fraction of the  $i$ th mode  $E_i$ , is defined as

$$E_i = \frac{\lambda_i}{\sum_{i=1}^N \lambda_i} \quad (7)$$

The temporal POD coefficients can be obtained by projecting  $\mathbf{U}$  onto  $\Phi_i$ :

$$a_i(t) = \Phi_i^* \mathbf{U} \quad (8)$$

The total number of POD modes ( $N$ ) is the rank of  $\mathbf{U}$ , which is usually equal to the number of snapshots considered. The PIV data contains 10 cardiac cycles with 18 instants per cycle, leading to 180 modes in total. For the CFD data, the flow field considered consists of only one cardiac cycle with 165 snapshots, resulting in 165 modes in total. The RPCA velocity field, on the other hand, consists of 180 snapshots since it was generated from PIV data, but consists of only 35 modes. This is because the RPCA process seeks to obtain a low-rank representation of the original data.

## 2.6 Reduced Order Model

To generate a low dimensional representation of the aortic flow under consideration, Equation 9 can be applied to reconstruct the flow field from the POD modes and the mean velocity  $\mathbf{u}(x, y)$  as:

$$\mathbf{u}(x, y, t) = \overline{\mathbf{u}(x, y)} + \sum_{i=1}^r a_i(t) \Phi_i(x, y) \quad (9)$$

where  $r$  denotes the number of modes included in the ROM. When setting  $r = N$ , where  $N$  denotes the total number of POD modes, Equation 9 yields FOM. Equivalently, the reconstructed snapshot matrix  $\mathbf{U}_r$  can be calculated from:

$$\mathbf{U}_r = \Phi_r \Sigma_r \Psi_r^* \quad (10)$$

with  $\Phi_r$ ,  $\Sigma_r$ , and  $\Psi_r$  are the truncated versions of  $\Phi$ ,  $\Sigma$ , and  $\Psi$ , respectively. The reconstruction error is defined as:

$$\varepsilon = \frac{\sum_{j=1}^m \sum_{i=1}^{2n} \left| \mathbf{U}(i, j) - \mathbf{U}_r(i, j) \right|}{\sum_{j=1}^m \sum_{i=1}^{2n} \left| \mathbf{U}(i, j) \right|} \times 100\% \quad (11)$$

The POD spatial structures and temporal coefficients were used to characterise specific flow features - *coherent structures* - in the pulsatile, aortic dissection flow, separating the periodic and random fluctuating structures from the mean flow. The spatial structures  $\Phi_i$  for the relevant modes were analysed by plotting the velocity fields. Then, the temporal characteristics of the flow were investigated by analysing the temporal coefficients of the most energetic POD modes in both the time and frequency domains.

Lastly, flow field reconstructions from the ROMs were performed according to Equation 9. First  $\mathbf{u}(x, y, t)$  was reconstructed using all the modes to verify the accuracy of the mathematical calculations. Then, they were reconstructed using only a selected number of modes (i.e.  $\Phi_1$ -2,  $\Phi_1$ -5, and  $\Phi_1$ -10) and the solution was compared to the original velocity fields, at different instants of the cardiac cycle, to quantify the differences.

Table 1: Percentage of Kinetic energy captured and reconstruction error of different groups of POD modes calculated from PIV velocity field, RPCA velocity field, and CFD velocity field

<i>Modes</i>	PIV POD		PIV RPOD		CFD POD	
	Energy(%)	Error(%)	Energy(%)	Error(%)	Energy(%)	Error(%)
1-2	86.33	34.18	98.15	13.10	95.52	19.54
1-5	89.57	30.16	99.37	7.85	98.77	10.18
1-10	91.72	27.06	99.78	4.60	99.72	4.81
all	~100	~0	~100	~0	~100	~0

### 3 Results and Discussion

#### 3.1 Kinetic energy distribution

Table 1 lists the cumulative kinetic energy contents of the POD and RPOD modes derived from the PIV data (PIV POD, PIV RPOD respectively) compared to those derived from the CFD data (CFD POD). The energy contained in the ROMs is expressed as a percentage of the total kinetic energy in their respective FOMs, i.e. the total energy of the original or filtered PIV and CFD velocity fields respectively. While more than 90% of the kinetic energy is reached within the first 2 modes for the PIV RPOD and CFD POD data, it takes 10 modes for the PIV POD to capture that amount of energy. Similarly, Table 1 also shows that the reconstruction errors from PIV RPOD and CFD POD converge to zero faster than the ones from PIV POD.

This is not surprising as the PIV data are subject to measurement noise. In contrast, the CFD velocity field was derived from numerical computations, no measurement errors are involved. Additionally, the use of a RANS model in CFD inherently ignores turbulent fluctuations, resulting in much cleaner data compared to PIV.

The RPCA process denoises the PIV data resulting in higher cumulative energy in the first two and ten modes compared to that from PIV data alone. The energy content of each mode becomes closer to that derived from the CFD data.

#### 3.2 POD structures and temporal coefficients

Selected POD structures ( $\Phi 1-3$ ) are shown in Figure 3 compared with the mean flow. All the first POD structures ( $\Phi 1$ ) show organised motion in the same direction as the mean flow which reflects the flow at the peak systolic phase (Franzetti et al., 2022). The structures extracted from PIV POD and PIV RPOD appear to be almost identical as they represent the most energetic flow features; they slightly differ from the CFD POD ones due to the differences between the measured and computed velocity fields discussed in our previous work (Bonfanti et al., 2020).

Modes 2 and 3 ( $\Phi 2-3$ ) exhibit more complex flow patterns characterised by re-circulation regions. As for  $\Phi 2$ , a high magnitude region can be seen at the inner side of the arch which reflects the flow pattern in diastole.

The temporal coefficients ( $a_i$ ) of the first three POD modes are shown in Figure 4 in the time (left column) and frequency domain (right column), respectively. The coefficients exhibit periodic characteristics in agreement with the literature (Kefayati and Poepping, 2013). The first temporal coefficient essentially reflects the shape of the patient-specific inlet flow waveform manifesting with a

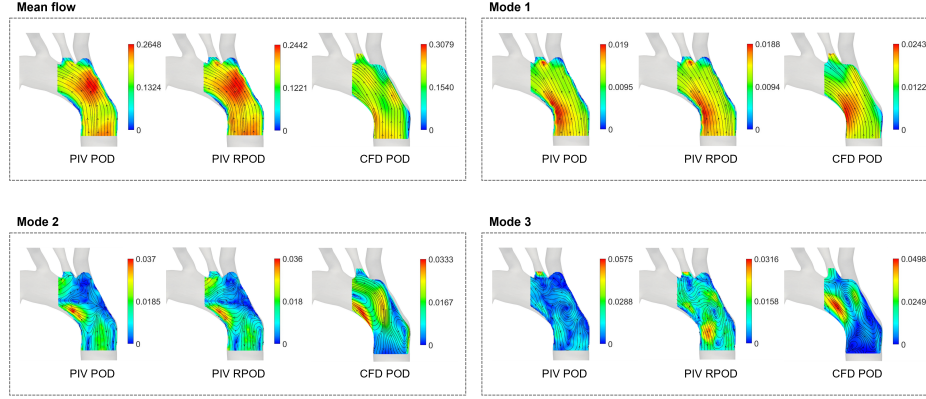


Figure 3: The mean velocity field and the first three POD structures ( $\Phi 1-3$ ) obtained from the PIV, RPCA, and CFD velocity fields, respectively. Super-imposed streamlines were used for illustration purposes, they do not convey any information on temporal variations. Please note that the scales of the contours are different.

dominant peak in the spectra at the frequency of the cardiac cycle ( $f = 73.2 \text{ bpm} = 1.22 \text{ Hz}$ ). As the number of modes increases, the temporal coefficients show more complicated patterns characterised by higher frequency oscillations. A second harmonic (2.44 Hz) is evident on the frequency spectra of the experimentally derived modes. This behaviour may be related to velocity fluctuations due to transitional flow. This behaviour is absent from the numerical POD coefficients which consist of one single cardiac cycle only, hence oscillating at the cardiac cycle frequency only.

### 3.3 Flow reconstructions

Figures 5-7 show the comparison between the FOMs at three instants of the cardiac cycle (peak systole, deceleration and diastole), and the reconstructed velocity fields of ROMs using  $\Phi 1-2$ ,  $\Phi 1-5$  and  $\Phi 1-10$ . The figure also shows contours of the differences in velocity magnitude between the original and reconstructed flow fields. The reconstruction errors are shown in Table 1. As expected, in all cases, the more POD/RPOD modes are included in the reconstruction, the lower the error.

The reconstructed flow fields from the PIV POD in Figure 5 show that good agreement can be achieved even using the first 2 POD modes at peak systole and in the descending part of the flow curve, where the flow follows relatively organised uni-directional patterns, with some differences occurring in near-wall re-circulation regions. However, more significant discrepancies are observed in diastole, both in terms of velocity magnitude, distribution and the flow directions indicated by the streamlines. Such differences are to be expected because, at diastole, the flow contains smaller vortical structures and a more complex flow field. To fully reconstruct these structures, a higher number of modes should be included. 10 modes appear to be sufficient to reconstruct the flow at diastole accurately. When reconstructing the flow with modes  $\Phi 1-10$ , the maximum absolute difference is about 0.09-0.10 m/s and occurs at systole.

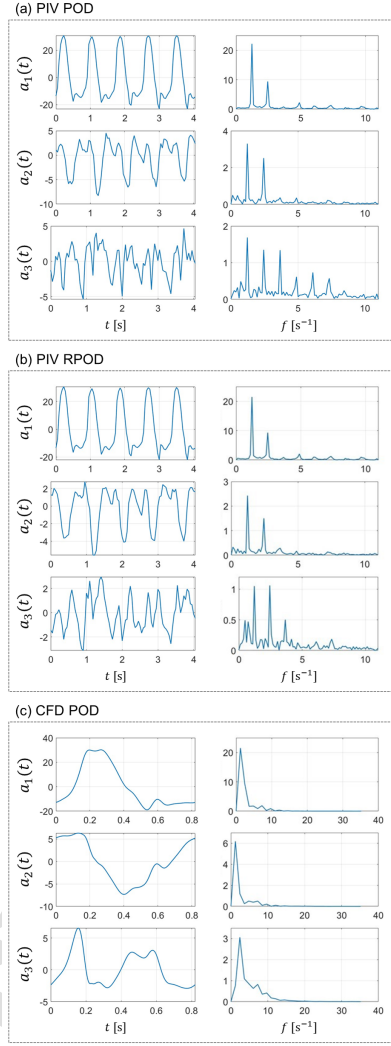


Figure 4: The first three POD temporal coefficients ( $a_1$ ,  $a_2$ , and  $a_3$ ) from (a) PIV POD, (b) PIV RPOD, and (c) CFD POD presented in (left) time domain and (right) frequency domain.



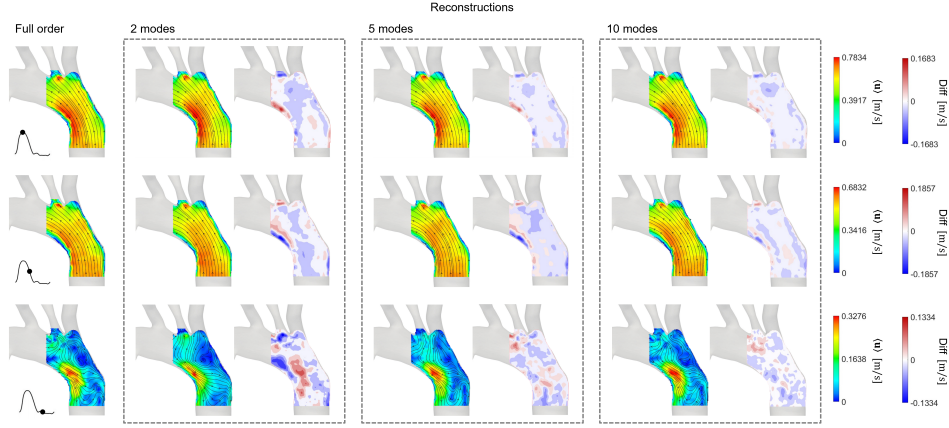


Figure 5: PIV POD, a POD reconstruction of PIV velocity field using  $\Phi 1-2$ ,  $\Phi 1-5$ , and  $\Phi 1-10$ . The FOM and reconstructed flow fields are visualised at three instances of the cardiac: peak systole, deceleration, and diastole. Contours showing the difference in velocity magnitude between the FOM and reconstructed flow fields are shown side by side with the reconstructed velocity field.

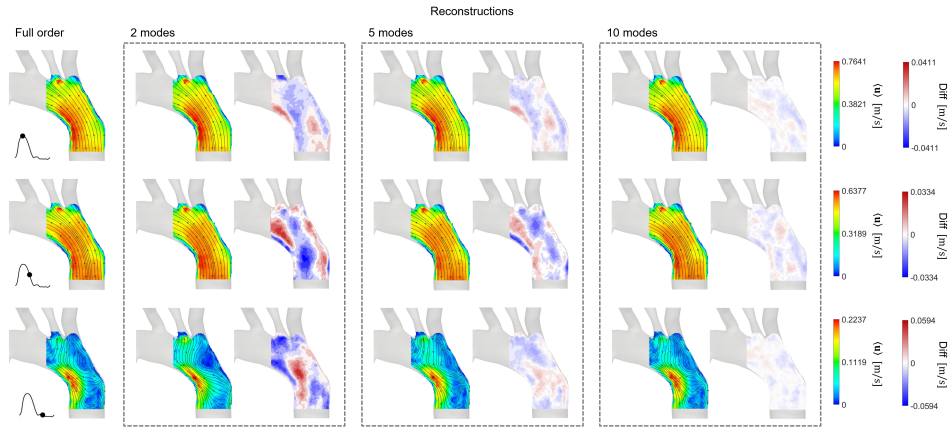


Figure 6: PIV RPOD, a POD reconstruction of RPCA velocity field using  $\Phi 1-2$ ,  $\Phi 1-5$ , and  $\Phi 1-10$ . The FOM and reconstructed flow fields are visualised at three instances of the cardiac: peak systole, deceleration, and diastole. Contours showing the difference in velocity magnitude between the FOM and reconstructed flow fields are shown side by side with the reconstructed velocity field.

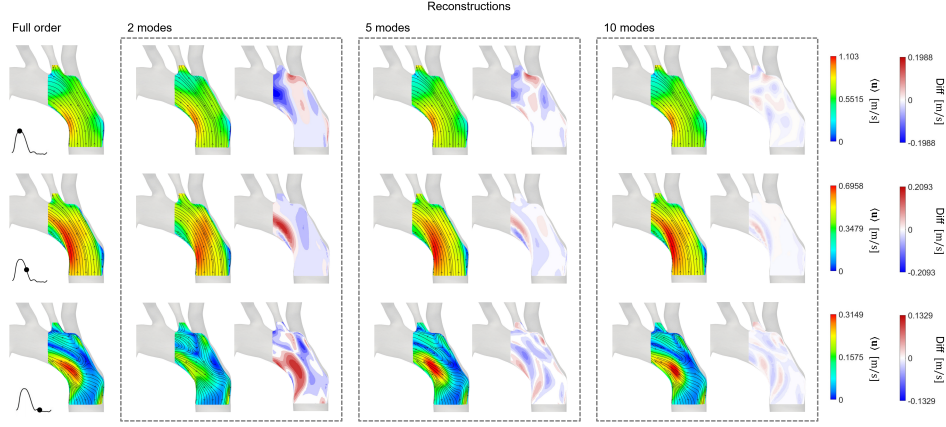


Figure 7: CFD POD, a POD reconstruction of CFD velocity field using  $\Phi_{1-2}$ ,  $\Phi_{1-5}$ , and  $\Phi_{1-10}$ . The FOM and reconstructed flow fields are visualised at three instances of the cardiac: peak systole, deceleration, and diastole. Contours showing the difference in velocity magnitude between the FOM and reconstructed flow fields are shown side by side with the reconstructed velocity field.

Similar reconstructed velocity fields are generally obtained from the PIV RPOD in Figure 6. The only noticeable difference is at diastole, where the RPCA velocity field exhibits lower velocity magnitudes compared to the PIV-derived one, due to its filtering action. The RPCA velocity magnitude ranges from 0 to 0.2237 m/s, while the original flow field from 0 to 0.3276 m/s at diastole. When using the same number of modes to reconstruct the flow field, PIV RPOD has a much lower reconstruction error than PIV POD. The maximum absolute error when using 10 modes for the flow reconstruction is only 0.007-0.008 m/s, i.e. 10 times lower than that in PIV POD.

Finally, Figure 7 shows that the flow reconstructions from the CFD POD analysis share similar important qualities with the experimental ones; namely that the first 2 modes are able to reconstruct the velocity field accurately at peak systole and deceleration phase, with the errors decreasing rapidly when more modes are included. The difference contour plots show less scatter compared to the PIV derived ones due to high spatial resolution of the numerical data. A maximum difference of around 0.05-0.06 m/s is found when reconstructing the flow fields using 10 modes; this is smaller than the errors in PIV POD but slightly higher than the case of PIV RPOD.

It is important to highlight that all the errors reported above are reconstruction errors. They are obtained by comparing the velocity fields from ROMs to those of their respective FOMs. These errors are not from comparisons among the PIV velocity fields, RPCA velocity fields, and CFD velocity fields (see Appendix A). Thus, they cannot be interpreted as such.

### 3.4 Towards personalised ROMs

The use of the RPCA algorithm in this study successfully filtered out high-frequency noise in the PIV data (see Figure 4), improving the performance of ROMs extracted from the data. In the context of

dimensionality reduction, the application of RPCA to PIV data leads to representations in a lower-dimensional space compared to the original PIV data. This feature of RPCA might be helpful when analysing the images from MR data for example, which would help paving the way towards the use of these numerical tools in a clinical setting.

However, RPOD may over-filter certain parts of the flow field as can be seen during diastole (Figure 5-7 bottom row). While the velocity magnitude of the PIV and CFD derived fields are in the same range, it is significantly lower (by about 30%) for the RPCA derived one. This shows that the algorithm may filter out some important flow features and if implemented in a real clinical pathway, might require careful consideration. This over-filtering issue can be addressed by increasing the value of the tuning parameter  $\lambda_1$ . However, too high a value of  $\lambda_1$  can lead to the presence of noise in the filtered data. Therefore, the main challenge involved in the application of RPCA is to find the optimal value of  $\lambda_1$  that appropriately filters out the unwanted motion while preserving the relevant ones. Future work can focus on fine tuning  $\lambda_1$  for a given dataset or exploring the integration of a physics-informed regularization term into the RPCA framework to preserve the velocity signal while still reducing noise.

Nevertheless, the enhancement of *in vitro*, experimental data using RPCA demonstrated here, suggests that such methods could potentially be applied to *in vivo* data, such as 4D flow MRI, to improve their quality, making them more amenable to computational modelling and flow reconstruction (Bakhshinejad et al., 2017; Fathi et al., 2018; Töger et al., 2020) for patient-specific studies. In addition, the ability of the RPCA algorithm to effectively clean data may also result in ROMs constructed from RPOD having to include fewer modes, leading to faster computations in their subsequent applications, which is an important feature if these techniques were to be incorporated in real clinical pathways.

This work also demonstrates that it is possible to represent the behaviour of complex, pathological aortic flows using ROMs consisting of only the first few POD/RPOD modes, which shows promise in the development of more computationally efficient models to support clinical decision-making. Examples include the works of Chang et al. (2017) who developed a computationally efficient ROM to study the flow patterns and the WSS distribution in simplified models of an abdominal aortic aneurysm, and Buoso et al. (2019), who developed ROMs of blood flow for non-invasive functional evaluation of the pressure drop in coronary artery disease using parameterised POD. ROMs may also possess properties that can serve as supplementary haemodynamic indices. For example, by monitoring the temporal evolution of energy distribution, it may be possible to track the progression of some cardiovascular diseases or even vascular remodelling. Moreover, the energy fraction associated with higher-order POD/RPOD modes may contain information that can be used to fine-tune turbulence parameters when modelling vascular flows.

Finally, ROMs can also be combined with rapidly evolving machine learning tools to allow for *optimization* and *design* in fluid mechanics, moving towards real-time modelling. This would allow, for instance, the study of a wide range of parameters for a given vascular pathology (e.g. increasing or decreasing the level of stenosis on coronary disease or coarctations) and to analyse the consequences on the flow and pressure fields, which could serve as an initial step to investigate patient-specific pre-interventional options (Siena et al., 2023; Pajaziti et al., 2022; Liang et al., 2020).

## 4 Conclusions

The time-dependent flow in an aortic model, measured by PIV, was enhanced by RPCA and decomposed by means of POD to create ROMs. The decomposed flows were compared against those from numerical data obtained for the same patient-specific conditions. The first two modes derived from

313 RPOD capture more than 90% of the kinetic energy, in agreement with the corresponding CFD derived  
314 ROMs.

315 The large and small-scale structures within the flow, corresponding to more or less energetic modes,  
316 were evaluated and described by means of POD/RPOD spatial structures and POD/RPOD temporal  
317 coefficients. By combining only the most energetic modes to represent the flow, it was shown that  
318 complex, time-dependent haemodynamic data can be represented with simpler low-dimensional models  
319 based on a small number of spatial modes. This combined with the strong reconstruction performance  
320 of RPOD, illustrates the potential of the approach to enhance the quality of measurements and to  
321 develop more computationally efficient models for clinical application.

## 322 CRediT authorship contribution statement

323 **Chotirawee Chatpattanasiri:** Conceptualisation, Formal analysis, Investigation, Methodology, Vi-  
324 sualisation, Writing-original draft. **Gaia Franzetti:** Conceptualisation, Formal analysis, Investi-  
325 gation, Methodology, Visualisation, Writing-original draft. **Mirko Bonfanti:** Investigation, Soft-  
326 ware. **Vanessa Diaz-Zuccarini:** Conceptualisation, Funding acquisition, Project administration,  
327 Resources, Supervision, Writing-review & editing. **Stavroula Balabani:** Conceptualisation, Funding  
328 acquisition, Project administration, Resources, Supervision, Writing-review & editing.

## 329 Conflict of interest

330 The authors declare that they have no known competing financial interests or personal relationships  
331 that could have appeared to influence the work reported in this paper.

## 332 Acknowledgements

333 This project was supported by the Wellcome/EPSRC Centre for Interventional and Surgical Sciences  
334 (WEISS) (203145Z/16/Z); the EPSRC Transformative Healthcare Technologies (EP/W00481X/1);  
335 the British Heart Foundation (FS/15/22/31356, NH/20/1/34705); UCLH Biomedical Research Centre  
336 (GA BRC636b/HEI/SB/1104); and the Department of Mechanical Engineering, University College  
337 London. The authors would also like to thank Dr. Tom Lacassagne and Dr. Andrea Ducci for their  
338 constructive feedback.

## 339 Appendix A. Comparison of velocity fields between CFD and 340 PIV before and after RPCA

341 The comparisons of PIV, RPCA, and CFD velocity fields is shown in Figure A1. Figure A1a shows  
342 the velocity magnitude of the mean flow in the three velocity fields with four straight lines. A closer  
343 comparison between the three velocity fields is provided in Figure A1b by plotting the axial velocity  
344 profiles ( $\langle \mathbf{u}_n \rangle$ ) over those four selected lines.

345 The percentage difference is calculated in the same way as in Bonfanti et al. (2020):

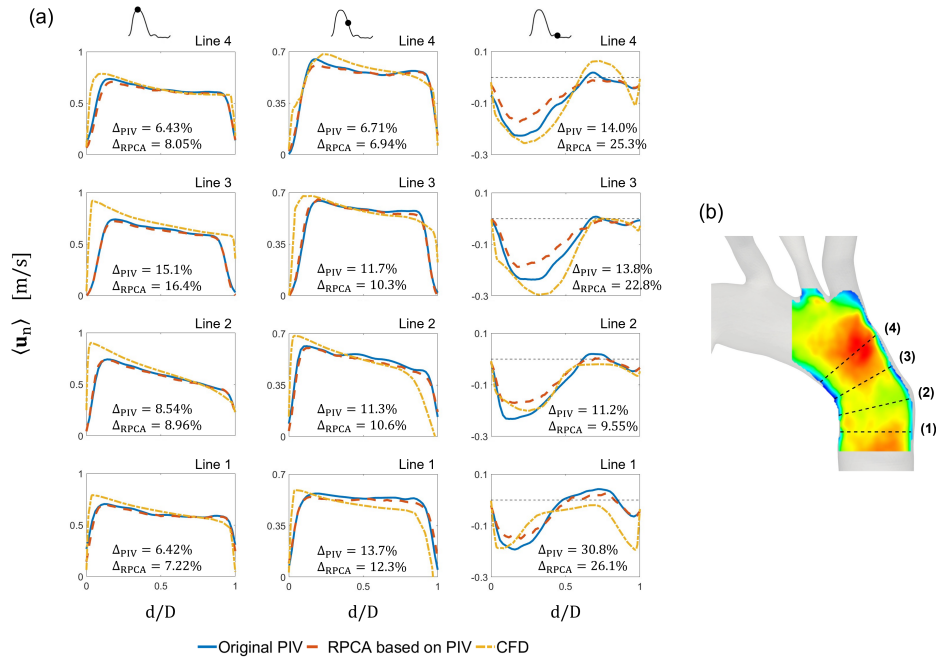


Figure A1: (a) Comparison of axial velocity profiles obtained from experimental PIV data before RPCA, after RPCA, and CFD data. (b) Four lines across the aortic arch where the velocity profiles were measured.

$$\Delta = \frac{1}{N} \sum_{i=1}^N \frac{|u_{n,j}^e - u_{n,j}^c|}{\max_j |u_{n,j}^c|} \quad (\text{A12})$$

where  $u_{n,i}^c$  is the CFD velocity profile. When calculating  $\Delta_{\text{PIV}}$ ,  $u_{n,i}^e$  is the PIV velocity profile, and when calculating  $\Delta_{\text{RPCA}}$ ,  $u_{n,i}^e$  is the RPCA velocity profile. It should be noted that the percentage differences are not exactly the same as those reported in Bonfanti et al. (2020) because there might be discrepancies in the locations of the four lines.

As shown from the above (Figure A1b), RPCA may not always bring the PIV and CFD closer together in terms of the actual velocity values due to the over-filtering behaviour discussed in Section 3.4. However, RPCA leads to PIV derived ROMs that capture the same percentage of energy as CFD ones when reconstructing with the same number of modes (Table1). To help visualise the effect of RPCA on PIV data, comparison can be found in the video file attached (or here.)

## Appendix B. normalised POD/RPOD coefficients

The relation between the first coefficients  $a_i$  was investigated by plotting the space  $(a_1^*, a_2^*)$ , calculated as:<sup>4</sup>

$$\tilde{a}_i = \frac{a_i}{\sqrt{2\lambda_i}} \quad (\text{B13})$$

and normalise as

$$a_i^* = \frac{2(\tilde{a}_i - \min(\tilde{a}_i))}{(\max(\tilde{a}_i) - \min(\tilde{a}_i))} - 1 \quad (\text{B14})$$

The normalised temporal coefficients  $a_1^*$ ,  $a_2^*$  and  $a_3^*$ , are plotted against each other in Figure B1. The phase-averaged coefficients for the experimental data are also indicated in blue. They exhibit organised, closed-loop structures, indicating periodicity similar to the CFD data.

The 2D plots of  $a_1^*$  and  $a_2^*$  in Figure B1 do not show a clear circular or elliptic pattern, implying that the first two POD modes do not form a pair. The plots also indicate the same behaviour for the first two PIV POD and PIV RPOD coefficients which slightly differs from the CFD POD ones.

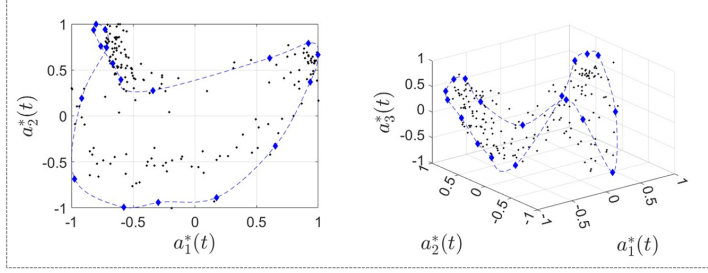
An interesting observation arises when investigating the relation amongst the first three coefficients ( $a_1^*$ ,  $a_2^*$  and  $a_3^*$ .) The plots on the right side of Figure B1a-c show a more complex organisation amongst these modes. This behaviour highlights the interdependent relationships and energy transfer between the first three modes and may correspond to energy transfer amongst different periodic structures (with different energy contents and frequency profiles) within the flow field. A similar ‘*triadic interaction*’ has been reported by Gabelle et al. (2017) in a stirred tank flow (who attributed the behaviour to non-linear interactions between the modes), and by Lacassagne et al. (2021) in an oscillating grid flow.

## References

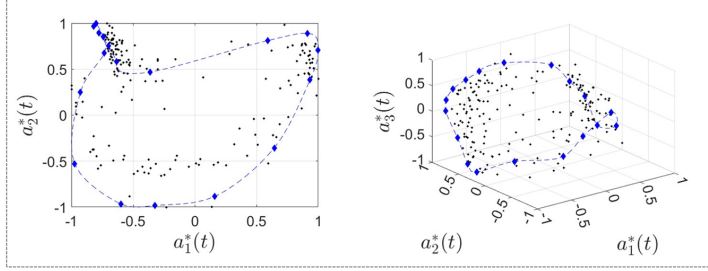
Arzani, A. and Dawson, S. T. (2021). Data-driven cardiovascular flow modelling: Examples and opportunities. *Journal of the Royal Society Interface*, 18.

<sup>4</sup>This approach has been used in different studies, for example see Imomoh et al. (2010) and Ducci et al. (2008).

(a) PIV POD



(b) PIV RPOD



(c) CFD POD

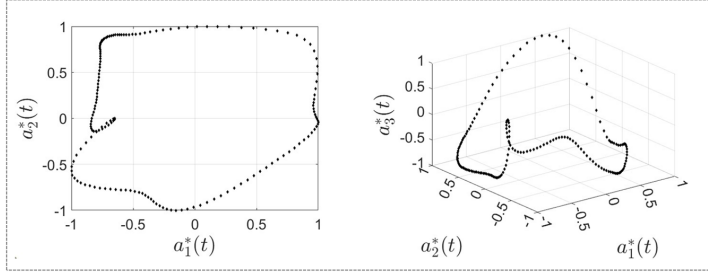


Figure B1: Scatter plots of normalised POD coefficients (left)  $a_1^*$  and  $a_2^*$  and (right)  $a_1^*$ ,  $a_2^*$  and  $a_3^*$  computed from (a) PIV POD, (b) PIV RPOD, and (c) CFD POD. The black points represent the coefficients for all the modes, whilst the blue ones represent the phase-averaged POD modes. The blue lines connect the phase-averaged coefficients for better visualisation.

- 375 Baghaie, A. (2019). Robust principal component analysis for background estimation of particle image  
376 velocimetry data. In *2019 IEEE Long Island Systems, Applications and Technology Conference*  
377 (*LISAT*), pages 1–6.
- 378 Bakhshinejad, A., Baghaie, A., Vali, A., Saloner, D., Rayz, V. L., and D’Souza, R. M. (2017). Merging  
379 computational fluid dynamics and 4D Flow MRI using proper orthogonal decomposition and ridge  
380 regression. *Journal of Biomechanics*, 58:162–173.
- 381 Ballarin, F., Faggiano, E., Ippolito, S., Manzoni, A., Quarteroni, A., Rozza, G., and Scrofani, R.  
382 (2016). Fast simulations of patient-specific haemodynamics of coronary artery bypass grafts based on  
383 a POD-Galerkin method and a vascular shape parametrization. *Journal of Computational Physics*,  
384 315:609–628.
- 385 Berkooz, G., Holmes, P., and Lumley, J. L. (1993). The proper orthogonal decomposition in the  
386 analysis of turbulent flows. *Annual review of fluid mechanics*, 25(1):539–575.
- 387 Bonfanti, M., Balabani, S., Alimohammadi, M., Agu, O., Homer-vanniasinkam, S., and Díaz-zuccarini,  
388 V. (2018). A simplified method to account for wall motion in patient-specific blood flow simulations  
389 of aortic dissection : Comparison with fluid-structure interaction. *Medical Engineering and Physics*,  
390 58:72–79.
- 391 Bonfanti, M., Franzetti, G., Homer-Vanniasinkam, S., Diaz-Zuccarini, V., and Balabani, S. (2020). A  
392 combined in vivo, in vitro, in silico approach to study the patient-specific haemodynamics of Type-B  
393 Aortic Dissections. *Annals of Biomedical Engineering*.
- 394 Brunton, S. L. and Kutz, J. N. (2019). *Data-Driven Science and Engineering: Machine Learning,*  
395 *Dynamical Systems, and Control*. Cambridge University Press.
- 396 Buoso, S., Manzoni, A., Alkadhi, H., Plass, A., Quarteroni, A., and Kurtcuoglu, V. (2019). Reduced-  
397 order modeling of blood flow for noninvasive functional evaluation of coronary artery disease. *Biome-*  
398 *chanics and Modeling in Mechanobiology*, 18(6):1867–1881.
- 399 Byrne, G., Mut, F., and Cebal, J. (2014). Quantifying the large-scale hemodynamics of intracranial  
400 aneurysms. *American Journal of Neuroradiology*, 35(2):333–338.
- 401 Candès, E. J., Li, X., Ma, Y., and Wright, J. (2011). Robust principal component analysis? *J. ACM*,  
402 58(3).
- 403 Chang, G. H., Schirmer, C. M., and Modarres-Sadeghi, Y. (2017). A reduced-order model for wall shear  
404 stress in abdominal aortic aneurysms by proper orthogonal decomposition. *Journal of Biomechanics*,  
405 54:33–43.
- 406 Chinesta, F., Ammar, A., Leygue, A., and Keunings, R. (2011). An overview of the proper general-  
407 ized decomposition with applications in computational rheology. *Journal of Non-Newtonian Fluid*  
408 *Mechanics*, 166(11):578–592.
- 409 Di Labbio, G. and Kadem, L. (2019). Reduced-order modeling of left ventricular flow subject to aortic  
410 valve regurgitation. *Physics of Fluids*, 31(3).
- 411 Ducci, A., Doulgerakis, Z., and Yianneskis, M. (2008). Decomposition of flow structures in stirred  
412 reactors and implications for mixing enhancement. *Industrial and Engineering Chemistry Research*,  
413 47(10):3664–3676.



- 414 Eivazi, H., Le Clainche, S., Hoyas, S., and Vinuesa, R. (2022). Towards extraction of orthogonal and  
415 parsimonious non-linear modes from turbulent flows. *Expert Systems with Applications*, 202:117038.
- 416 Farahbakhsh, I. (2020). *Krylov Subspace Methods with Application in Incompressible Fluid Flow*  
417 *Solvers*. John Wiley & Sons.
- 418 Fathi, M. F., Bakhshinejad, A., Baghaie, A., Saloner, D., Sacho, R. H., Rayz, V. L., and D'Souza,  
419 R. M. (2018). Denoising and spatial resolution enhancement of 4D flow MRI using proper orthogonal  
420 decomposition and lasso regularization. *Computerized Medical Imaging and Graphics*, 70:165–172.
- 421 Febina, J., Sikkandar, M. Y., and Sudharsan, N. (2018). Wall shear stress estimation of thoracic  
422 aortic aneurysm using computational fluid dynamics. *Computational and mathematical methods in*  
423 *medicine*, 2018.
- 424 Franzetti, G., Bonfanti, M., Homer-Vanniasinkam, S., Diaz-Zuccarini, V., and Balabani, S. (2022).  
425 Experimental evaluation of the patient-specific haemodynamics of an aortic dissection model using  
426 particle image velocimetry. *Journal of Biomechanics*, 134.
- 427 Franzetti, G., Díaz-Zuccarini, V., and Balabani, S. (2019). Design of an in vitro mock circulatory loop  
428 to reproduce patient-specific vascular conditions: Toward precision medicine. *Journal of Engineering*  
429 *and Science in Medical Diagnostics and Therapy*, 2.
- 430 Gabelle, J. C., Morchain, J., and Liné, A. (2017). Kinetic Energy Transfer between First Proper Or-  
431 thogonal Decomposition Modes in a Mixing Tank. *Chemical Engineering and Technology*, 40(5):927–  
432 937.
- 433 Han, S., Schirmer, C. M., and Modarres-Sadeghi, Y. (2020). A reduced-order model of a patient-  
434 specific cerebral aneurysm for rapid evaluation and treatment planning. *Journal of Biomechanics*,  
435 103:109653.
- 436 Hellmeier, F., Nordmeyer, S., Yevtushenko, P., Bruening, J., Berger, F., Kuehne, T., Goubergrits, L.,  
437 and Kelm, M. (2018). Hemodynamic evaluation of a biological and mechanical aortic valve prosthesis  
438 using patient-specific mri-based cfd. *Artificial organs*, 42(1):49–57.
- 439 Imomoh, E., Dusting, J., and Balabani, S. (2010). On the quasiperiodic state in a moderate aspect  
440 ratio Taylor-Couette flow. *Physics of Fluids*, 22(4):1–10.
- 441 Javadzadegan, A., Moshfegh, A., Afrouzi, H. H., and Omid, M. (2018). Magnetohydrodynamic blood  
442 flow in patients with coronary artery disease. *Computer Methods and Programs in Biomedicine*,  
443 163:111–122.
- 444 Kefayati, S. and Poepping, T. L. (2013). Transitional flow analysis in the carotid artery bifurcation by  
445 proper orthogonal decomposition and particle image velocimetry. *Medical Engineering and Physics*,  
446 35(7):898–909.
- 447 Lacassagne, T., Simoëns, S., El Hajem, M., and Champagne, J.-Y. (2021). Pod analysis of oscillating  
448 grid turbulence in water and shear thinning polymer solution. *AIChE Journal*, 67(1):e17044.
- 449 Liang, L., Mao, W., and Sun, W. (2020). A feasibility study of deep learning for predicting hemody-  
450 namics of human thoracic aorta. *Journal of Biomechanics*, 99.

- 451 Liang, Y., Lee, H., Lim, S., Lin, W., Lee, K., and Wu, C. (2002). Proper orthogonal decomposition  
452 and its applications—part i: Theory. *Journal of Sound and vibration*, 252(3):527–544.
- 453 Murata, T., Fukami, K., and Fukagata, K. (2020). Nonlinear mode decomposition with convolutional  
454 neural networks for fluid dynamics. *Journal of Fluid Mechanics*, 882.
- 455 Pajaziti, E., Montalt-Tordera, J., Capelli, C., Sivera, R., Sauvage, E., Schievano, S., and Muthurangu,  
456 V. (2022). Deep neural networks for fast acquisition of aortic 3d pressure and velocity flow fields.  
457 *arXiv preprint arXiv:2208.12156*.
- 458 Quarteroni, A. and Rozza, G. (2007). Numerical Solution of Parametrized Navier–Stokes Equations  
459 by Reduced Basis Methods. *Numerical Methods for Partial Differential Equations*, 23(November  
460 2013):904–922.
- 461 Rigatelli, G., Chiastra, C., Pennati, G., Dubini, G., Migliavacca, F., and Zuin, M. (2021). Applications  
462 of computational fluid dynamics to congenital heart diseases: a practical review for cardiovascular  
463 professionals. *Expert Review of Cardiovascular Therapy*, 19(10):907–916.
- 464 Scherl, I., Strom, B., Shang, J. K., Williams, O., Polagye, B. L., and Brunton, S. L. (2020). Robust  
465 principal component analysis for modal decomposition of corrupt fluid flows. *Physical Review Fluids*,  
466 5.
- 467 Schmid, P. J. (2021). Annual review of fluid mechanics dynamic mode decomposition and its variants.  
468 *Annu. Rev. Fluid Mech.* 2022, 54:225–254.
- 469 Siena, P., Girfoglio, M., Ballarin, F., and Rozza, G. (2023). Data-driven reduced order modelling  
470 for patient-specific hemodynamics of coronary artery bypass grafts with physical and geometrical  
471 parameters. *Journal of Scientific Computing*, 94(2):1–30.
- 472 Stokes, C., Bonfanti, M., Li, Z., Xiong, J., Chen, D., Balabani, S., and Díaz-Zuccarini, V. (2021). A  
473 novel mri-based data fusion methodology for efficient, personalised, compliant simulations of aortic  
474 haemodynamics. *Journal of Biomechanics*, 129.
- 475 Stokes, C., Haupt, F., Becker, D., Muthurangu, V., von Tengg-Kobligk, H., Balabani, S., and Díaz-  
476 Zuccarini, V. (2023). The influence of minor aortic branches in patient-specific flow simulations of  
477 type-b aortic dissection. *Annals of Biomedical Engineering*.
- 478 Töger, J., Zahr, M. J., Aristokleous, N., Markenroth Bloch, K., Carlsson, M., and Persson, P. O.  
479 (2020). Blood flow imaging by optimal matching of computational fluid dynamics to 4D-flow data.  
480 *Magnetic Resonance in Medicine*, 84(4):2231–2245.
- 481 Wang, Y., Yao, H., and Zhao, S. (2016). Auto-encoder based dimensionality reduction. *Neurocomput-*  
482 *ing*, 184:232–242.

Conflict of Interest Statement

## Declaration of Competing Interest

The authors declare that they have no known competing financial interests or personal relationships that could have appeared to influence the work reported in this paper.